Article

Not peer-reviewed version

Temporal and Spatial Dynamics in Alluvial Floodplain Wetlands Associated with Extreme Climatic Events

Carina Cristiane Korb *, Laurindo Antonio Guasselli *, Thiago Bazzan, Tássia Fraga Belloli, Ananda Müller Postay de Lima, Ana Lucia Freitas

Posted Date: 15 May 2026

doi: 10.20944/preprints202605.0994.v1

Keywords: extreme events; remote sensing; alluvial–colluvial floodplain wetlands; principal component analysis; Sinos River; environmental conservation

 doi:10.20944/preprints202605.0994.v1

Article

Temporal and Spatial Dynamics in Alluvial Floodplain Wetlands Associated with Extreme Climatic Events

Carina Cristiane Korb [1,*], Laurindo Antonio Guasselli [1,*], Thiago Bazzan [2], Tássia Fraga Belloli [1], Ananda Müller Postay de Lima [1] and Ana Lucia Freitas [1]

[1] Laboratory of Geoprocessing and Environmental Analysis (LAGAM), Institute of Geosciences, Postgraduate Program in Remote Sensing, Federal University of Rio Grande do Sul (UFRGS), Porto Alegre 91509-900, Rio Grande do Sul, Brazil

[2] National Center for Monitoring and Alerts of Natural Disasters (CEMADEN), São José dos Campos 12247-016, São Paulo, Brazil

* Correspondence: carinac.korb@gmail.com (C.C.K.); laurindo.guasselli@ufrgs.br (L.A.G.)

Abstract

Floodplain wetlands are dynamic and biodiverse environments that provide important ecosystem services. This study analyzes the temporal and spatial dynamics of hydrogeomorphological attributes, vegetation, and water in floodplain wetlands. The methodology consisted of applying PCA in temporal (T) and spatial (S) modes, decomposing spectral indices (NDVI, NDMI, MNDWI) to identify variability patterns associated with ENSO events. The results revealed that C2 was the main descriptor of hydrological anomalies, with strong temporal synchrony between vegetation vigor (NDVI) and the expansion of the water surface (MNDWI), contrasting with the water stress response captured by NDMI. PCA highlighted environmental heterogeneity within the floodplain, with peatland areas standing out as zones of high spatial complexity and greater water retention capacity. Temporal variability responded primarily to climatic extremes, whereas spatial variability was modulated by hydrogeomorphology.

Keywords: extreme events; remote sensing; alluvial–colluvial floodplain wetlands; principal component analysis; Sinos River; environmental conservation

1. Introduction

Wetlands located in the alluvial floodplains of large rivers are among the most productive and biodiverse ecosystems on the planet, performing vital ecological and socioeconomic functions. [1]. Regulated by flood pulse periodicity, these environments are characterized as highly dynamic fluvial systems [1,2]. This hydrological variation sustains habitat heterogeneity, making these environments essential components for the conservation of regional biodiversity [2–4].

The diversity of ecosystem services offered by these ecosystems emphasizes their strategic importance for preserving ecological integrity [5]. However, these ecosystems are threatened by impacts of varying magnitudes. Global climate change, particularly extreme events, and land cover changes constitute the main drivers of their degradation [6–8].

Extreme hydrological events, such as floods and droughts, can compromise wetland functions and induce hydrogeomorphological changes, with impacts on biodiversity and their carbon storage capacity [6,9,10]. The hydrological regulation services provided by wetlands during flood periods influence flow patterns, reduce flood volume, attenuate peak discharge, and help control excess water within river channels. Studies suggest the importance of flooding for vegetation productivity in inundated areas [11]. During dry periods, wetlands help maintain baseflow and recharge groundwater, thereby enhancing watershed resilience to hydrological extremes [12,13].

 doi:10.20944/preprints202605.0994.v1

Difficult access to wetlands is one of the main factors driving the use of remote sensing data, supported by the high revisit frequency of satellites and their economic feasibility [14,15]. Spectral indices derived from optical sensors enable the quantification of hydrogeomorphological variables (vegetation, water, soils) that reveal patterns of spatial and temporal variability. These indicators provide insights into the conservation status and ecological health of these ecosystems in the face of environmental disturbances associated with extreme events [16].

Principal Component Analysis (PCA) applied to multitemporal image series allows the synthesis of data variability, isolating seasonal changes from structural alterations in the landscape [17–19]. This statistical transformation is effective in reducing information redundancy, highlighting the axes of greatest variance that describe the system dynamics [20,21], making it suitable for monitoring wetlands across multiple scales [22–27]. Some studies have applied PCA in T-Mode (temporal) and S-Mode (spatial), for example in seasonally flooded areas [28,29] and in coastal wetlands [30]. However, the application of PCA to understand wetland dynamics in response to extreme events remains limited.

In southern Brazil, the El Niño–Southern Oscillation (ENSO) is the main driver of interannual climate variability [30,31]. However, the magnitude of extreme events may exceed the typical phases of this phenomenon. In 2024, the state of Rio Grande do Sul, Brazil, was impacted by a hydrological event of historic proportions during a transition toward climatic neutrality. The persistence of frontal systems and atmospheric blocking resulted in exceptional rainfall volumes [32].

Based on these considerations, this study aims to analyze the temporal and spatial dynamics of vegetation and water, as hydrogeomorphological attributes, using remote sensing in alluvial floodplain wetlands in response to extreme climatic events in the Sinos River basin, southern Brazil.

2. Materials and Methods

2.1. Study Area

The Sinos River basin drains an area of 3,694 km², located in the Metropolitan Region of Porto Alegre (RMPA), in Rio Grande do Sul, southern Brazil. The basin landscape is composed of six geomorphological units: Serra Geral, the Campos Gerais Plateau, the Serra Geral Escarpments, the Jacuí River Depression, the Lagoon Plain, and the Alluvial–colluvial Plain [33]. Relief in the upper reaches is characterized by high elevations, exceeding 1,000 m, whereas in the middle and lower reaches, flat and low-lying areas susceptible to flooding occur at elevations ranging from 20 to 5 m.

The vegetation cover is part of the Atlantic Forest biome and presents a mosaic of phytophysiognomies that vary along the topographic gradient, including Submontane Semideciduous Seasonal Forest, Lowland Forest, and Pioneer Formations [34]. The upper reach contains wetlands of small extent (0.1 to 5 ha), whereas in the middle and lower reaches, the low slope favors channel widening and a greater concentration of wetlands. In these segments, these ecosystems exhibit larger dimensions and greater hydrological complexity [35,36] associated with the flat relief of the Alluvial–colluvial Plain. This sector exhibits higher urban occupation, which exerts pressure on the remaining wetlands and amplifies the impacts during flood events [37].

Regional precipitation ranges from 1,100 to 1,800 mm annually, with peaks in winter and spring, under a subtropical climate regime. The hydrological regime is controlled by the interaction between the Tropical Maritime (mT) and Polar Maritime (mP) air masses and is also influenced by ENSO. El Niño episodes result in above-average precipitation, whereas La Niña events induce hydrological deficits [38,39].

Between 2020 and 2022, the persistence of the La Niña phenomenon imposed extreme climatic conditions that resulted in three years of severe droughts and a pronounced hydrological deficit [40]. This scenario, intensified by elevated temperatures, compromised the resilience of wetlands, drastically reducing saturation levels and altering their hydrological dynamics. Between 2023 and 2024, extreme climatic conditions resulted in severe flooding associated with the El Niño phenomenon. In 2023, two events occurred in September and November [41], and between April 27

 doi:10.20944/preprints202605.0994.v1

and May 13, 2024, a hydrological event of historic magnitude affected Rio Grande do Sul. Intense rainfall, associated with El Niño conditions and exceptionally warm sea surface temperatures in the equatorial Atlantic Ocean, impacted the region, with more than 600 mm of precipitation recorded [42]. The occurrence of exceptional rainfall, combined with the natural susceptibility of the terrain and dense urbanization, resulted in severe flooding that drastically affected municipalities in the RMPA. Water levels exceeded historical thresholds, redefining the extent of floodplains in the region and highlighting its socio-environmental vulnerability.

As a case study, the analyzed wetlands are located in the middle reach of the main channel of the Sinos River basin, within the Alluvial–colluvial Plain compartment (Figure 1). The spatial extent was defined using the flood extent in the middle reach (lower Sinos River), recorded during the 2024 extreme hydrological event. In this section, the lithology consists of alluvial and colluvial sediments, such as gravel, sand, silt, and clay, as well as peat formations [43,44], with elevations below 10 m. Poorly drained soils predominate, classified as Haplic Eutrophic Planosols, typical of flood-prone lands with clayey texture [45], under vegetation cover consisting of remnants of Semideciduous Seasonal Forest. In this section of the basin, part of the wetlands is under legal protection, forming part of the conservation unit known as the Municipal Natural Park Banhado da Imperatriz.

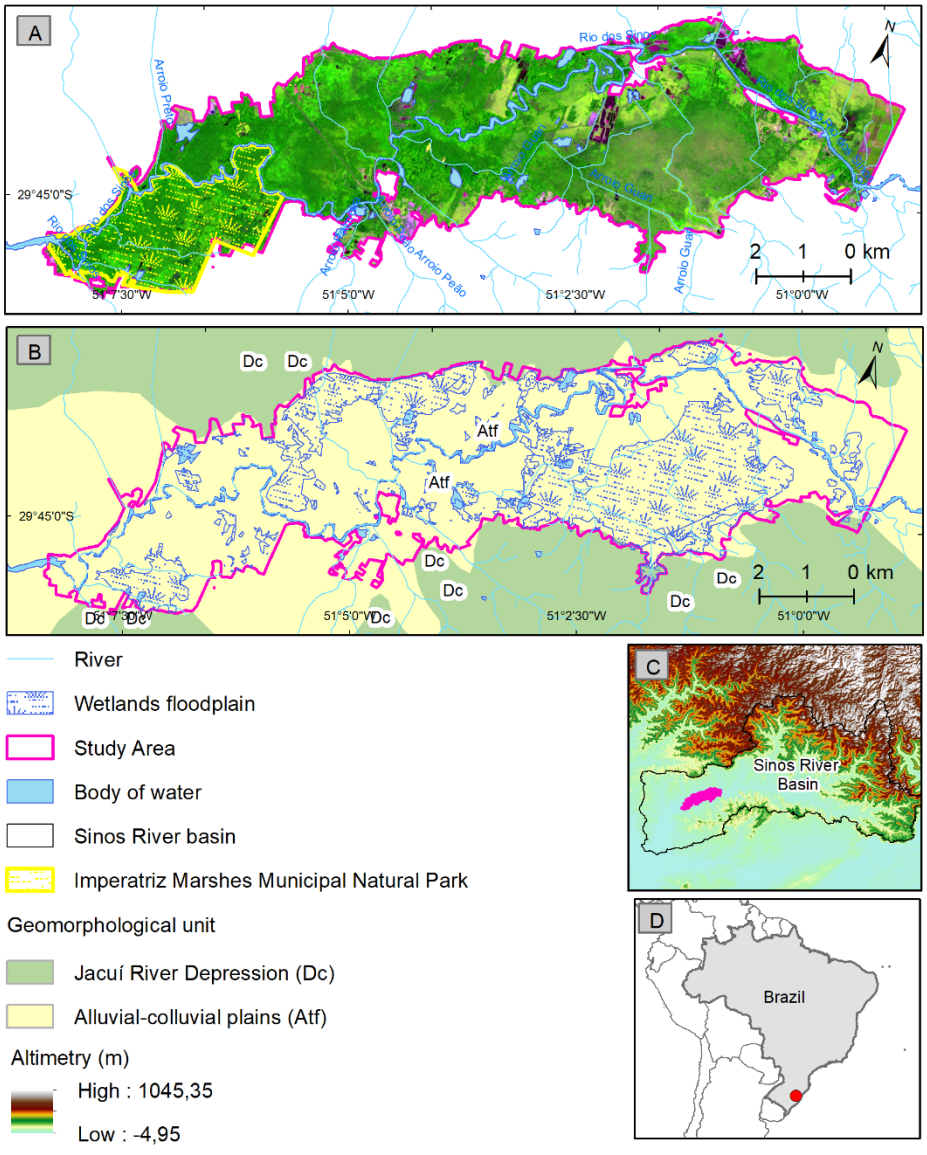

 doi:10.20944/preprints202605.0994.v1

Figure 1. Location of the study area: (A) Sentinel-2 false-color composite R3G8B4; rivers and watershed [46]; (B) Geomorphological Units [44]; Wetlands [47,48]; (C) Elevation [49]; (D) Political boundaries [43,45].

2.2. Data and Procedures

In this study, the following cartographic datasets were used: (a) geomorphological compartmentalization [33,43]; (b) vegetation cover [34]; (c) the 2024 flood extent [50]; (d) precipitation data from the Climate Hazards Group InfraRed Precipitation with Stations (CHIRPS) product, obtained using JavaScript-based scripts in the Code Editor of Google Earth Engine (GEE); and (e) evapotranspiration data from the Terra Moderate Resolution Imaging Spectroradiometer (MODIS) product, MOD16A2GF, obtained through the GEE platform.

Multispectral images from the Sentinel-2 satellite, MSI (Multispectral Instrument) sensor, were used for the period 2019–2024, with a spatial resolution of 10 m, obtained via the GEE platform. One image per month was selected for each year of the time series, covering the four climatic seasons and different phases of ENSO variability (El Niño, La Niña, and Neutral).

Spectral indices representing hydrogeomorphological attributes were computed in the GEE platform (Table 1): the Normalized Difference Vegetation Index (NDVI) and the Normalized Difference Moisture Index (NDMI) for vegetation, and the Modified Normalized Difference Water Index (MNDWI) for water. The time series consisted of 72 images for each index.

Table 1. Spectral indices used in the study.

Hydrogeomorphological attribute / Variable	Formula	Reference
Normalized Difference Vegetation Index (NDVI)	$\frac{(red - green)}{(red + green)}$	[51]
Normalized Difference Moisture Index (NDMI)	$\frac{(NIR - SWIR1)}{(NIR + SWIR1)}$	[52]
Modified Normalized Difference Water Index (MNDWI)	$\frac{(green - SWIR1)}{(green + SWIR1)}$	[53]

2.3. Principal Component Analysis (PCA)

The analysis of wetland variability was conducted by decomposing the time series (2019–2024) of spectral indices using PCA, standardized and non-centered, with T-mode (temporal) and S-mode (spatial) orientations. In T-mode, the variables are temporal samples, allowing the identification of recurring spatial patterns over time. In S-mode, the variables are spatial samples, enabling the identification of recurring temporal patterns across space [27–51].

PCA was performed using the TerrSet Libera GIS software, specifically the Earth Trends Modeler (ETM) module [54]. In T-mode, outputs included principal component images, variance explained, eigenvalues, and component loadings; in S-mode, variance, loading images, and score profiles were obtained. Four principal components were derived: C1, C2, C3, and C4.

To better understand and highlight the variability of vegetation and water, we analyzed color composites of the principal components (C2, C3, C4), as C1 represents the dominant pattern. Temporal and spatial variations of interest are better captured by the secondary componentes, particularly C2, as they reflect contrasts and heterogeneities not explained by C1. Therefore, C2 was used for analyses in both T-mode and S-mode.

The assessment of the dependency relationship between vegetation dynamics and water availability was carried out through statistical analyses applied to the PCA results. For T-mode, the loadings of C2 were used to represent the temporal variability of the indices across the 72 images of the historical series. For S-mode, the analysis focused on the C2 scores to describe the spatial distribution of attributes within the study area.

Normality in both modes was assessed using the Shapiro–Wilk and Kolmogorov–Smirnov tests with Lilliefors correction. The results indicated that the NDVI, NDMI, and MNDWI variables did not follow a normal distribution ($p < 0.05$), exhibiting skewness and kurtosis typical of dynamic

 doi:10.20944/preprints202605.0994.v1

hydrological environments. Given the rejection of the normality hypothesis, the strength of association between the spectral indices was measured using Spearman's rank correlation coefficient (p). This non-parametric method was selected for its robustness to non-Gaussian distributions and its ability to assess monotonic relationships based on ranks, ensuring greater reliability in interpreting spatial co-occurrence (S-mode) and temporal synchrony (T-mode) between vegetation vigor and water content. All statistical analyses were performed using STATISTICA software.

3. Results

3.1. Temporal (T-Mode) and Spatial (S-Mode) Dynamics

The analyzed period is marked by a severe hydroclimatological contrast: between 2020 and 2022, the region experienced three consecutive years of drought with a pronounced hydrological deficit, followed by a cycle of extreme flooding in September and November 2023. This scenario culminated in May 2024 with a hydrological event of historic magnitude in Rio Grande do Sul.

Analysis of the variance explained and eigenvalues (Table 2) in this time series shows that the first component (C1) is dominant across all indices, accounting for 95.34%, 88.21%, and 92.34% of the variation in NDVI, NDMI, and MNDWI, respectively, with high loading values.

Table 2. Percentage of variance and eigenvalues associated with each Principal Component and hydrogeomorphological attribute, T-Mode.

Index	T-Mode Component	C1	C2	C3	C4
NDVI	% Variance	95.34	2.75	0.35	0.25
	T-Mode Eigenvalue	68.64	1.98	0.25	0.18
NDMI	% Variance	88.21	2.68	2.19	0.93
	T-Mode Eigenvalue	63.51	1.93	1.58	0.67
MNDWI	% Variance	92.34	4.89	0.79	0.37
	T-Mode Eigenvalue	66.48	3.52	0.57	0.27

The PCA results in T-mode allowed the identification of spatial patterns of vegetation and water in wetlands of the Alluvial–colluvial Plain in response to these recurring events over time. The T-mode loading profiles of the spectral indices (Figure 2) show that PC1 maintains a constant loading close to 1, representing the structural pattern of the landscape, whereas C2 exhibits greater variability, acting as the main descriptor of temporal anomalies in wetlands.

Between January 2019 and August 2023, C2 shows small fluctuations in NDVI and MNDWI (Figure 2a,c), coinciding with periods of severe drought associated with La Niña. However, NDMI, which indicates vegetation and soil moisture levels, shows that during this period wetlands maintained moisture conditions with responses reflected in vegetation health.

Between the second half of 2023 and May 2024, when precipitation extremes associated with El Niño occurred, peaks in MNDWI loadings (Figure 2c) indicate increased surface water presence and soil saturation, accompanied by corresponding increases in NDVI (Figure 2a) and reductions in NDMI (Figure 2b). This behavior reflects the rapid response dynamics of wetlands to large flood pulses, and although part of the vegetation becomes submerged, it promotes increased vegetation vigor during subsequent flood recession periods.

 doi:10.20944/preprints202605.0994.v1

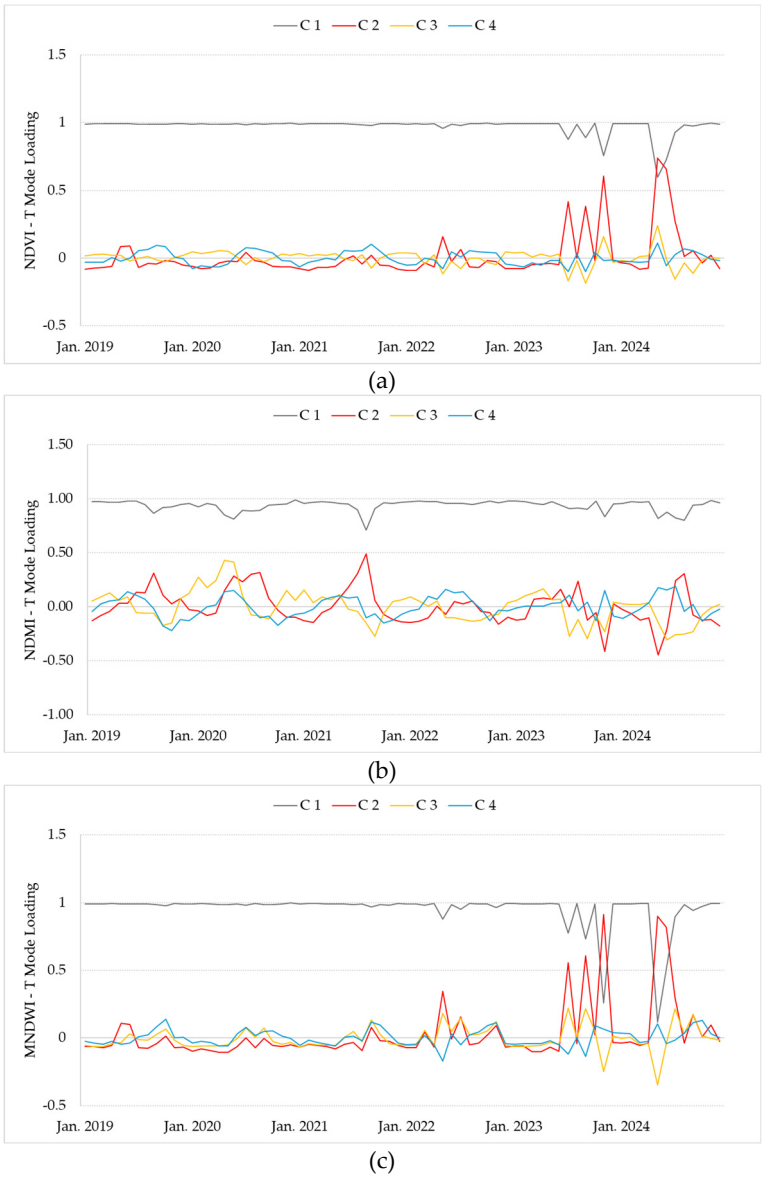

Figure 2. T-Mode loading profiles of the spectral indices (a) NDVI; (b) NDMI; (c) MNDWI. The black, red, green, and blue lines correspond to temporal variation (C1, C2, C3, C4).

The color composite images of components C2, C3, and C4 (Figure 3) reveal spatial patterns that recur over time (T-Mode), reflecting distinct temporal responses of vegetation and water in wetland environments. In the NDVI (Images 1, 2, 3), NDMI (Images 5, 6, 7), and MNDWI (Images 8, 9, 10), component C2 dominates the variability of the spectral indices. The greatest variation in vegetation response occurs in areas predominantly covered by aquatic macrophytes, influenced by the exceptional flood pulse associated with the extreme 2024 event. In Frames C and D, there is a stronger shared influence with component C3.

 doi:10.20944/preprints202605.0994.v1

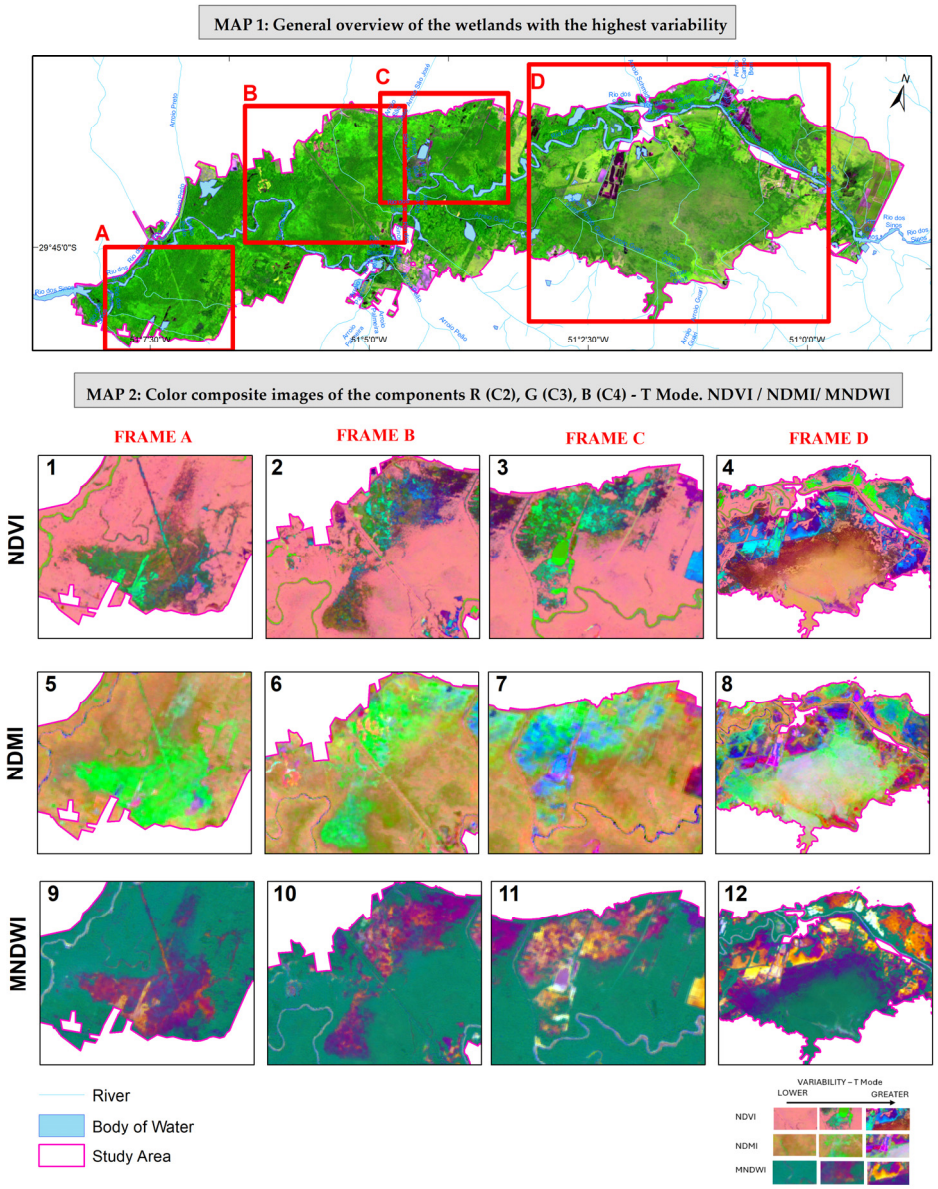

Figure 3. Color composite of components C2, C3, and C4 (T-Mode) for the spectral indices NDVI (1, 2, 3, 4); NDMI (5, 6, 7, 8); and MNDWI (9, 10, 11, 12).

Frame D (Images 4, 8, 12) stands out as the sector with the highest temporal complexity, characterized by the predominance of vegetation associated with peatland environments. Components C3 and C4 play a significant role across all three indices, suggesting dynamics more strongly controlled by seasonality and local land cover conditions. This results in a heterogeneous spectral signature that is less directly linked to the main flood pulse of the Alluvial–colluvial Plain. In peatland areas, vegetation tends to overlap zones of water accumulation with varying residence times or responds to lower-magnitude precipitation events without equivalent effects on vegetation vigor.

The PCA results in S-Mode highlight temporal patterns of hydrogeomorphological attributes that are spatially recurrent across the wetlands. The percentage of variance explained and the eigenvalues indicate that component C1 represents the dominant spatial pattern for all attributes, accounting for 93.87%, 86.95%, and 90.44% of the variability in NDVI, NDMI, and MNDWI, respectively, with proportionally high scores (Table 3).

 doi:10.20944/preprints202605.0994.v1

Table 3. Percentage of variance and eigenvalues associated with each Principal Component and hydrogeomorphological attribute, S-Mode.

Index	S-Mode Component	C1	C2	C3	C4
NDVI	% Variance	93.87	2.56	0.64	0.34
	S-Mode Eigenvalue	4597016.75	125414.79	31120.92	16588.01
NDMI	% Variance	86.95	3.73	2.06	0.68
	S-Mode Eigenvalue	425783.22	18248.04	10084.75	3333.52
MNDWI	% Variance	90.44	5.51	0.58	0.42
	S-Mode Eigenvalue	442874.57	26997.20	2851.63	2054.25

The S-Mode loading profiles (Figure 4) show the temporal contribution of each image in the time series to the definition of spatial patterns of hydrogeomorphological attributes in wetlands. Component C1 exhibits high and variable loadings across all indices (NDVI, NDMI, MNDWI), in contrast to the T-Mode, highlighting the greater spatial variability of moisture across the landscape throughout the analyzed period.

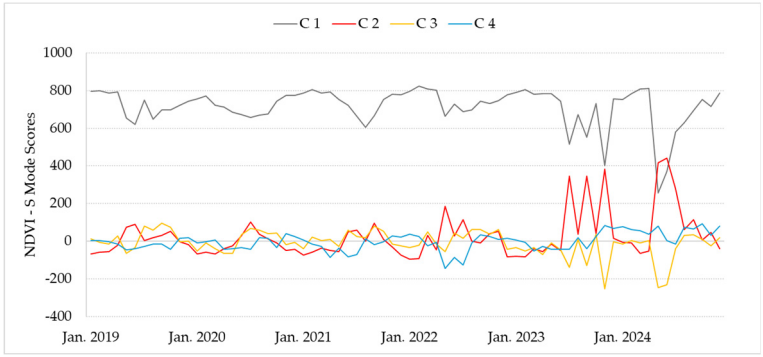

(a)

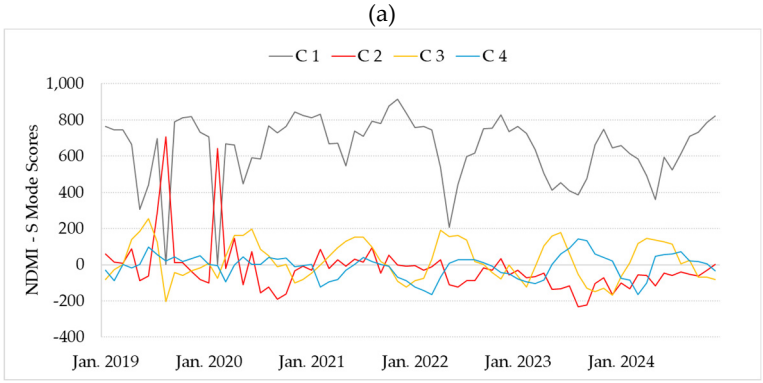

(b)

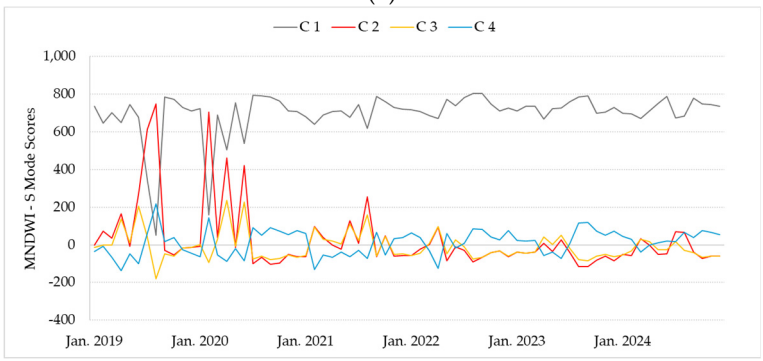

(c)

Figure 4. S-Mode loading profiles of the spectral indices: (a) NDVI; (b) NDMI; and (c) MNDWI. The black, red, green, and blue lines represent the temporal variation of components C1, C2, C3, and C4, respectively.

 doi:10.20944/preprints202605.0994.v1

Component C2 stands out by exhibiting pronounced loading peaks, revealing periods when the spatial variability of wetlands was most intense. In the NDVI (Figure 4a), C2 peaks are concentrated from late 2023 onward, reaching a maximum in May 2024, indicating that the spatial pattern of vegetation vigor was strongly reorganized by the extreme flood event. In the NDMI (Figure 4b) and MNDWI (Figure 4c) profiles, C2 displays an inverse behavior since the beginning of the series (2019 and 2020), associated with the prolonged La Niña period. Components C3 and C4 remain close to zero for most of the time, acting only during localized, lower-magnitude episodes, reinforcing the role of C2 as the primary component responding to hydrological anomalies.

The color composite images of components C2, C3, and C4 (Figure 5) highlight spatial patterns (S-Mode) that recur across the Alluvial–colluvial Plain, delineating sectors of greatest contrast and variability associated with the hydrogeomorphological heterogeneity of wetlands.

In the NDVI (Images 1, 2, 3), NDMI (Images 5, 6, 7), and MNDWI (Images 8, 9, 10), the predominance of component C2 in structuring spatial variability is evident, indicating that the main observed gradients are associated with moisture distribution and hydrological connectivity across the floodplain.

Across all three spectral indices, Frames C and D exhibit more complex spatial patterns, suggesting the joint influence of secondary variability components, particularly C3 and C4. This behavior indicates the presence of zones with differing saturation conditions and water residence times, associated with local controls such as microtopography, water accumulation, and variations in vegetation cover, which modulate the spectral response in a more heterogeneous manner.

Frame D (Images 4, 8, 12) stands out as the sector with the highest spatial complexity, where the relative contribution of secondary components is most evident across all indices. This pattern suggests an area with high hydrogeomorphological heterogeneity, possibly associated with vegetation adapted to persistently saturated conditions, such as peatland environments.

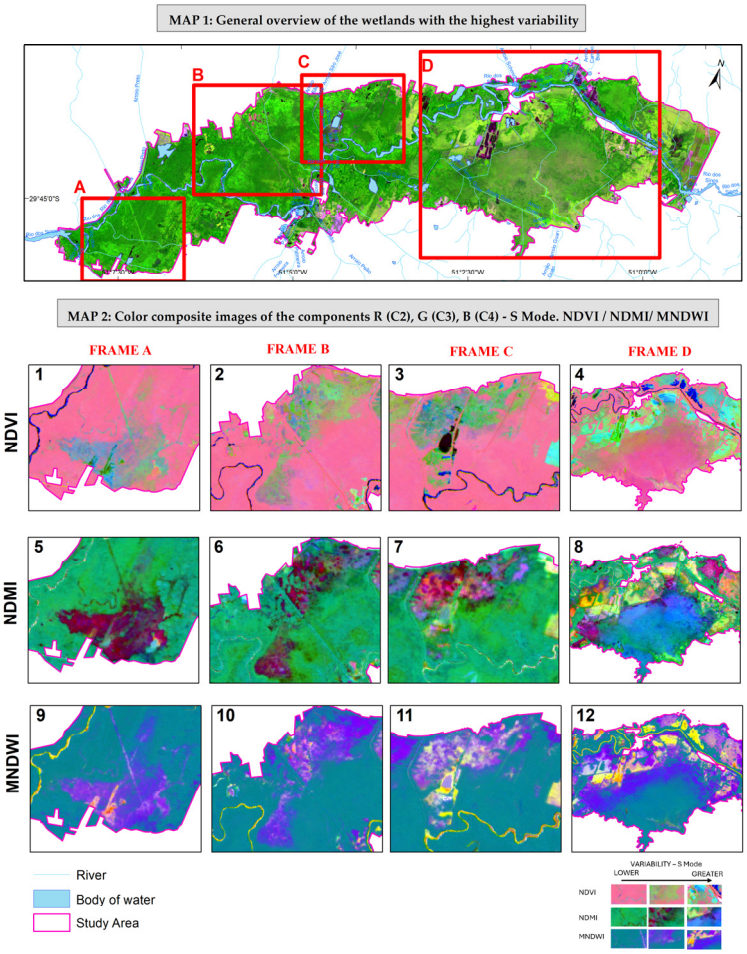

 doi:10.20944/preprints202605.0994.v1

Figure 5. Color composite of components C2, C3, and C4 (S-Mode) for the spectral indices NDVI (1, 2, 3, 4); NDMI (5, 6, 7, 8); and MNDWI (9, 10, 11, 12).

3.2. Relationship Between the Hydrogeomorphological Attributes of Vegetation and Water

Spearman correlation coefficients, applied to the T-Mode loadings and S-Mode scores for C2, reveal statistically significant associations ($p < 0.001$) across all combinations of indices analyzed (Tables 4 and 5). This statistical significance supports the analysis of interdependencies between vegetation vigor and hydrological dynamics at both temporal and spatial scales of the component.

Table 4. Spearman Correlation Matrix – C2, T-Mode.

	NDVI	NDMI	MNDWI
NDVI	1,0000	0,3478	0,6327
NDMI	0,3478	1,0000	-0,2763
MNDWI	0,6327	-0,2763	1,0000

Table 5. Spearman Correlation Matrix – C2, S-Mode.

	NDVI	NDMI	MNDWI
NDVI	1,0000	-0,2891	-0,1909
NDMI	-0,2891	1,0000	0,6084
MNDWI	-0,1909	0,6084	1,0000

The Spearman correlation matrices for C2 (Tables 4 and 5) reveal distinct dynamics between the T-Mode and S-Mode scales. In T-Mode, a moderate to strong positive correlation is observed between NDVI and MNDWI ($p = 0.6327$), suggesting that, over time, periods of higher vegetation vigor coincide with increased surface moisture or expansion of open water. In contrast, S-Mode presents an inverse relationship, showing a negative correlation between NDVI and MNDWI ($p = -0.1909$) and, simultaneously, a strong positive correlation between NDMI and MNDWI ($p = 0.6084$).

Linear regression lines applied to the T-Mode loadings (Figure 6a,b) reveal the temporal behavior of the variables in relation to the hydrological dynamics captured by C2. A strong positive linear trend is observed between NDVI and MNDWI (Figure 6a), with the regression model explaining 95.1% ($R^2 = 0.951$) of the variability in vegetation vigor based on variations in the water index. This high coefficient of determination suggests temporal synchrony: periods of greater water availability or wetland expansion coincide with increased spectral response of photosynthetically active vegetation. In contrast, the relationship between NDMI and MNDWI (Figure 6b) shows a negative and significantly weaker linear trend, with MNDWI explaining 19.2% ($R^2 = 0.192$) of the variability in NDMI loadings.

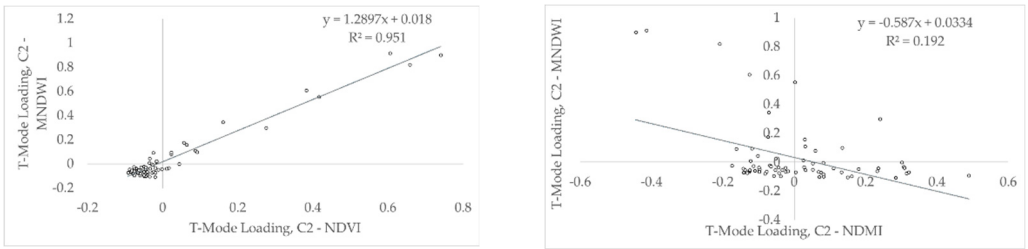

(a) (b)

Figure 6. Scatter plots of vegetation and water spectral indices for C2 (T-Mode). (a) NDVI (dependent variable) and MNDWI (predictor variable); (b) NDMI (dependent variable) and MNDWI (predictor variable).

For S-Mode, which analyzes spatial variation, the results show a reversal compared to T-Mode. Linear regression lines for S-Mode scores (Figure 7a,b) indicate a significant shift in the spatial relationship between spectral indices within C2. The spatial variability of NDVI is not explained by

 doi:10.20944/preprints202605.0994.v1

variations in MNDWI (Figure 7a), presenting an R^2 of 0.017 (1.7%) and a slightly negative trend line. This result indicates that, geographically, the presence of photosynthetically active vegetation does not follow a linear pattern relative to the occurrence of surface water, suggesting spatial independence between vegetation vigor and open water.

On the other hand, a strong positive linear association is observed between NDMI and MNDWI (Figure 7b), with the regression model explaining 74.1% ($R^2 = 0.7409$) of the spatial variability. Unlike what is observed at the temporal scale, the geographic distribution of areas with higher leaf moisture content (NDMI) is strongly coupled with the presence of surface moisture or saturated soils as captured by MNDWI. This pattern suggests that, within the spatial domain of C2, vegetation water content is the primary indicator associated with the distribution of water across the Alluvial–colluvial Plain.

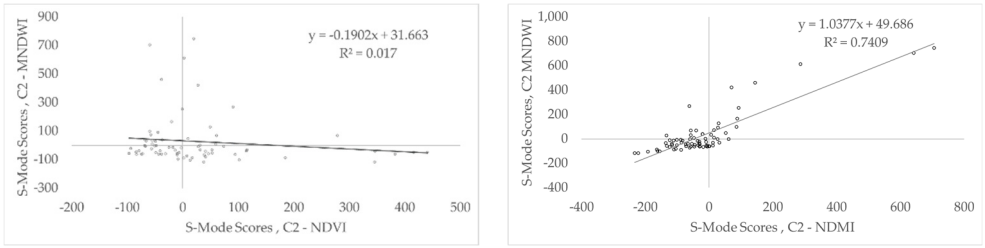

(a) (b)

Figure 7. Scatter plots of vegetation and water spectral indices for C2 (S-Mode). (a) NDVI (dependent variable) and MNDWI (predictor variable); (b) NDMI (dependent variable) and MNDWI (predictor variable).

3.3. Water Balance

The temporal and spatial analysis of C2, compared with water balance variables between 2019 and 2024 (Figure 4), reveals a sensitive response of spectral indices to climatic seasonality and extreme hydrological events. In T-Mode (Figure 8a,c,e), NDVI and MNDWI loadings show greater synchrony with precipitation peaks and periods of positive water balance, reaching historically high magnitudes between the second half of 2023 and the first half of 2024. This period, marked by extreme flooding in the Sinos River basin, is clearly isolated by C2, where MNDWI captures the expansion of open water surfaces and NDVI reflects the vigorous increase in biomass in response to excess water.

The evapotranspiration (ET) curve exhibits a more stable behavior and is seasonally lagged relative to precipitation peaks. It is observed that sharp declines in spectral indices occur during intervals when ET exceeds precipitation, resulting in a negative water balance (represented by the lower yellow bars). In S-Mode (Figure 8b,d,f), the scores indicate that, even under irregular precipitation conditions, NDMI and MNDWI maintain a close relationship in identifying areas with higher moisture retention across the floodplain.

T-Mode Loading: S-Mode Scores:

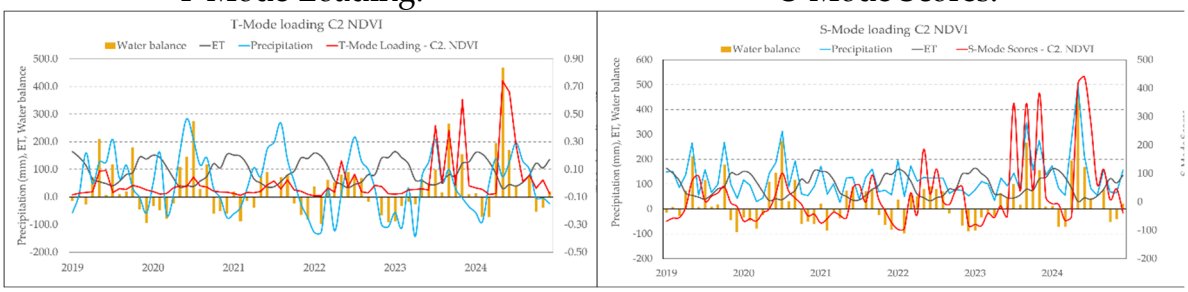

(a) (b)

 doi:10.20944/preprints202605.0994.v1

Figure 8. Estimated values of precipitation, evapotranspiration, and water balance from 2019 to 2024. C2 loadings and scores by hydrogeomorphological attribute, presented for both T-Mode and S-Mode analyses. NDVI (a,b), NDMI (c,d), MNDWI (e,f).

4. Discussion

The interpretation of the PCA reveals that the Alluvial–colluvial Plain of the Sinos River operates under a complex pulse regime, where the temporal and spatial dynamics of T-Mode and S-Mode converge to highlight the susceptibility of wetlands to hydrological extremes. Component C2 suggests that extreme events, such as the floods of 2023 and 2024, override the baseline temporal and spatial patterns (C1), temporarily reconfiguring the spectral signature of biomass and the dynamics of water retention.

While parts of Frames A and B exhibit responses linked to floodplain wetlands, the heterogeneity observed in Frame D, characterized by the presence of organic soils (peat), shows a greater capacity for water retention and attenuation of flood pulses. This configuration indicates that hydrogeomorphological dynamics in wetlands are not uniform, but rather governed by a combination of topographic variation, vegetation typology, and resilience to alternating prolonged water deficits and extreme flooding [54]. Studies indicate that during drought periods, a combination of drought tolerance and dormancy strategies enables vegetation to recover after dry conditions and recolonize areas previously invaded by terrestrial species [55].

In Frame D, vegetation vigor and leaf water content in peatland areas [56] operate under a distinct regime of temporal and spatial variability compared to other wetlands. In general, however, vegetation responses differ depending on their position relative to inundated areas [11].

This pattern allows the identification of core zones within the Alluvial–colluvial Plain, where hydric stress drives vegetation vigor [57] and leaf water content in subsequent periods. This dynamic reveals the resilience of wetlands to hydrological fluctuations throughout the time series [58,59]. Despite the occurrence of La Niña droughts or El Niño-driven floods, such as the 2024 event, these sectors preserved their biophysical and functional identity, demonstrating a capacity for recovery and maintenance of wetland conditions that distinguish them from adjacent zones.

Although PCA has already been applied in wetland studies [16,20,21,24,27,60,61], the combined exploration of matrices in T-Mode and S-Mode in alluvial plain systems to isolate temporal and spatial signatures of extreme events remains underexplored in the literature. Typically, wetland studies using PCA rely on multispectral bands [24,60] and spectral mixture models [27]. In addition,

 doi:10.20944/preprints202605.0994.v1

the use of spectral index time series has linked principal components to biophysical parameters of vegetation cover via NDVI and EVI [20,21], or to water body dynamics through MNDWI [62].

Our study employed multitemporal decomposition in T (temporal) and S (spatial) modes of spectral index images representing two hydrogeomorphological attributes: water and vegetation. Complementarily, this time–space decomposition provided insights into temporal dynamics across the historical series [17], revealing that the water radiometric index (MNDWI) acts as an important predictor of vegetation dynamics when considering NDVI, in contrast to the negative trend observed for NDMI.

The negative trend observed in NDMI, contrasted with the strong predictive capability of MNDWI, suggests a decoupling between surface water availability and leaf water content during extreme events. While MNDWI captures the expansion of open water surfaces (flood pulse), the negative response of NDMI may be associated with submergence of marsh vegetation or physiological stress due to anoxia, which compromises leaf water content even under saturated soil conditions. This divergence reinforces that, in alluvial plains under complex pulse regimes, biomass moisture (NDMI) is not a linear indicator of hydrology (MNDWI), but rather an ecophysiological response mediated by species tolerance to water residence time [63–65].

Hydrological extremes associated with El Niño and La Niña governed the coupling between biomass productivity and hydrological dynamics. The integrated analysis revealed that this interdependence is not uniform, but modulated by temporal signatures of extreme hydrological events, as well as by vegetation patterns and typologies. Wetlands attenuate extreme floods and mitigate severe droughts; however, their type and spatial distribution influence their regulatory capacity and the degree to which they buffer such events [12,13]. During severe droughts, wetlands can alleviate downstream water scarcity by releasing stored water, whereas the efficiency of flood regulation largely depends on their water storage capacity [13].

Climate projections based on General Circulation Models (GCMs), which have demonstrated high skill in simulating historical ENSO episodes, indicate an increasing frequency of extreme El Niño and La Niña events. Under 21st-century global warming scenarios, the recurrence of these phenomena is expected to intensify, exacerbating hydrological variability in wetlands [66].

Water availability and temperature are critical climatic variables that regulate biogeochemical processes and, consequently, the ecosystem services provided by wetlands [67]. n these environments, the balance between positive and negative interactions with the climate system determines the efficiency of carbon balance in ecosystems that function as global carbon sinks [10,67].

The synchrony observed between T-Mode loadings (NDVI and MNDWI) and peaks of water surplus in 2023–2024 highlights the hydrogeomorphological role of flood pulses, where hydrology acts as a forcing mechanism of primary productivity in the Alluvial–colluvial Plain [1,40]. The floods that occurred between 2023 and 2024, of historical magnitude, not only expanded open water surfaces (MNDWI) but also triggered a vigorous increase in biomass (NDVI), demonstrating that the flood pulse regulates biogeochemical processes and ecological succession in wetlands.

The relative stability of evapotranspiration (ET) in contrast to precipitation variability suggests an ecophysiological control mechanism, where declines in spectral indices during periods of negative water balance indicate thresholds of vegetation tolerance to hydric stress. Due to relatively weaker hydrological connections with surface waters, such as river channels, wetland hydrology is primarily governed by fluctuations in the water table, controlled by precipitation, evapotranspiration, and basin inputs [68,69]. Conversely, the spatial persistence of moisture revealed by S-Mode demonstrates that pedogeomorphological controls play a buffering role, preserving critical ecosystem functions even under irregular precipitation regimes [10,67].

The spatial persistence identified by S-Mode, even under irregular precipitation regimes, indicates that the Alluvial–colluvial Plain of the Sinos River functions as an environmental buffer.

In this context, our results indicate that wetlands within the floodplain exhibit self-regulation mechanisms in response to hydrological extremes, acting as a dynamic regulatory system. The preservation of resilient sectors, such as peatland zones, becomes strategic in light of the projected

 doi:10.20944/preprints202605.0994.v1

intensification of El Niño and La Niña cycles. Understanding these ecophysiological and hydrogeomorphological responses is therefore essential for maintaining ecosystem functions and for managing water sustainability at the regional scale under the uncertainties of global climate change.

5. Conclusions

The application of PCA, structured in T- and S-Modes, proved to be a robust tool for decoding the hydrogeomorphological complexity of wetlands located in alluvial plains. The integration of time series of spectral indices (NDVI, NDMI, and MNDWI) allowed the identification of recurrent temporal and spatial patterns, as well as the variability of responses induced by hydrological events of historical magnitude. The results showed that the Alluvial–colluvial Plain of the Sinos River exhibits heterogeneous environmental susceptibility, where floodplain dynamics and the presence of organic soils (peat) play a decisive role in the effects of droughts and extreme floods, such as those recorded during the 2020–2024 cycle.

T-Mode was instrumental in linking the spatial configuration of the floodplain to specific climatological events, demonstrating that the exceptional flood pulse of 2024 altered the spectral signature of wetlands, while S-Mode revealed the internal compartmentalization of the system.

The identification of distinct hydrological response units, particularly in Frame D, shows that the technique is capable of distinguishing between general variability patterns in wetlands and localized responses controlled by microtopography and the presence of peat soils.

Although vegetation structure (NDVI) and leaf water content (NDMI) share seasonal trajectories, they exhibit distinct response scales to flood pulses, highlighting the functional complexity inherent to wetlands in the Alluvial–colluvial Plain.

While vegetation vigor shows a medium-term response to hydrological variations, water stress captured by NDMI reveals immediate sensitivity, especially in transitional zones. In contrast, surface water dynamics (MNDWI) exhibit greater spatial heterogeneity, indicating that flooding is not governed solely by precipitation, but also controlled by geomorphological factors and the presence of organic soils (peat). This variability in index responses reinforces the need for multivariate approaches to map susceptibility and resilience capacity in these ecosystems under extreme climatic events.

In T-Mode, the moderate to strong positive correlation between NDVI and MNDWI suggests that, over time, periods of higher vegetation vigor coincide with increased surface moisture or expansion of open water. S-Mode, in contrast, presents an inverse relationship, showing a negative correlation between NDVI and MNDWI and, simultaneously, a strong positive correlation between NDMI and MNDWI. A strong positive linear trend is observed between NDVI and MNDWI, whereas a negative and significantly weaker trend is found between NDMI and MNDWI.

The modulation of spectral index variability in wetlands of the Alluvial–colluvial Plain of the Sinos River clearly reflects the alternation between ENSO phases. During the La Niña period (2020–2022), a systematic suppression in C1 loadings for NDMI and MNDWI was observed, associated with prolonged water deficit affecting vegetation moisture and reducing water surface extent. Conversely, the transition to El Niño conditions (2023–2024) was marked by pronounced C2 loading peaks, capturing the exceptional magnitude of flood pulses and the subsequent shift in vegetation phenological response (NDVI). This demonstrates that climatic extremes act as key drivers of wetland environmental dynamics, pushing the system beyond its typical seasonal variability.

These results have important implications for land-use planning and the management of conservation units in the lower Sinos River. The delineation of sectors with distinct water residence times and high environmental susceptibility can support improved wetland conservation, particularly in protected areas such as the Parque Natural Municipal Banhado da Imperatriz. Understanding the role of these areas as buffers and water retention zones during high-magnitude events reinforces the need for their full preservation, the definition of priority areas for ecological restoration, and the implementation of early warning systems based on the spectral behavior of vegetation and soil under conditions of water deficit or excess.

 doi:10.20944/preprints202605.0994.v1

Author Contributions: C.C.K.: conception, research, methodology, mapping, validation, data preparation, investigation, analysis, and writing of the article; L. A. G.: supervision, research, validation, review, analysis, and writing of the article; T.B.: validation, review, analysis, and writing of the article; T. F.B.: review, analysis, and writing of the article; A.M.P.L.: review; A.L.F.: review.

Funding: Research funded by the Foundation for Research Support of the State of Rio Grande do Sul (FAPERGS) - Research and Development Program Focused on Climate Disasters, Grant Agreement 24/255-0002149-3; CNPq PQ scholarship—process number 301822/2022-0.

Institutional Review Board Statement: Not applicable.

Data Availability Statement: All data generated or analyzed during this study are included in this published article. More detailed data can be provided upon request to the corresponding author.

Acknowledgments: To the Postgraduate Program in Remote Sensing of the State Center for Research in Remote Sensing and Meteorology/UFRGS; to CNPQ and FAPERGS for their financial support.

Conflicts of Interest: The authors declare no conflicts of interest.

References

1. Junk, W.J.; Bayley, P.B.; Sparks, R.E. Flood Pulse Concept in River- Floodplain-Systems.; **1989**; Vol. 106, pp. 110–127.
2. Jing, L.; Zeng, Q.; He, K.; Liu, P.; Fan, R.; Lu, W.; Lei, G.; Lu, C.; Wen, L. Vegetation Dynamic in a Large Floodplain Wetland: The Effects of Hydroclimatic Regime. *Remote Sensing* **2023**, *15*, doi:10.3390/rs15102614.
3. Arthington, A.H.; Godfrey, P.C.; Pearson, R.G.; Karim, F.; Wallace, J. Biodiversity Values of Remnant Freshwater Floodplain Lagoons in Agricultural Catchments: Evidence for Fish of the Wet Tropics Bioregion, Northern Australia. *Aquatic Conservation: Marine and Freshwater Ecosystems* **2015**, *25*, 336–352, doi:10.1002/aqc.2489.
4. Pander, J.; Mueller, M.; Geist, J. Habitat Diversity and Connectivity Govern the Conservation Value of Restored Aquatic Floodplain Habitats. *Biological Conservation* **2018**, *217*, 1–10, doi:10.1016/j.biocon.2017.10.024.
5. Ostrowski, A.; Connolly, R.M.; Sievers, M. Evaluating Multiple Stressor Research in Coastal Wetlands: A Systematic Review. *Marine Environmental Research* **2021**, *164*, 105239, doi:10.1016/j.marenvres.2020.105239.
6. Day, J.W.; Christian, R.R.; Boesch, D.M.; Yáñez-Arancibia, A.; Morris, J.; Twilley, R.R.; Naylor, L.; Schaffner, L.; Stevenson, C. Consequences of Climate Change on the Ecogeomorphology of Coastal Wetlands. *Estuaries and Coasts* **2008**, *31*, 477–491, doi:10.1007/s12237-008-9047-6.
7. Cunha, C.N. da; Piedade, M.T.F.; Junk, W.J. *Classificação e Delineamento Das Áreas Úmidas Brasileiras e de Seus Macrohabitats*; EdUFMT: Brasil, Cuiabá - MT, 2015; ISBN 978-85-327-0557-0.
8. He, Q.; Li, Z.; Daleo, P.; Lefcheck, J.S.; Thomsen, M.S.; Adams, J.B.; Bouma, T.J. Coastal Wetland Resilience through Local, Regional and Global Conservation. *Nat. Rev. Biodivers.* **2025**, *1*, 50–67, doi:10.1038/s44358-024-00004-x.
9. Erwin, K.L. Wetlands and Global Climate Change: The Role of Wetland Restoration in a Changing World. *Wetlands Ecol Manage* **2009**, *17*, 71–84, doi:10.1007/s11273-008-9119-1.
10. Salimi, S.; Almuktar, S.A.A.A.N.; Scholz, M. Impact of Climate Change on Wetland Ecosystems: A Critical Review of Experimental Wetlands. *Journal of Environmental Management* **2021**, *286*, 112160, doi:10.1016/j.jenvman.2021.112160.
11. Ivory, S.J.; McGlue, M.M.; Spera, S.; Silva, A.; Bergier, I. Vegetation, Rainfall, and Pulsing Hydrology in the Pantanal, the World's Largest Tropical Wetland. *Environ. Res. Lett.* **2019**, *14*, 124017, doi:10.1088/1748-9326/ab4ffe.
12. Wu, Y.; Sun, J.; Jun Xu, Y.; Zhang, G.; Liu, T. Projection of Future Hydrometeorological Extremes and Wetland Flood Mitigation Services with Different Global Warming Levels: A Case Study in the Nenjiang River Basin. *Ecological Indicators* **2022**, *140*, 108987, doi:10.1016/j.ecolind.2022.108987.

 doi:10.20944/preprints202605.0994.v1

13. Wu, Y.; Sun, J.; Hu, B.; Zhang, G.; Rousseau, A.N. Wetland-Based Solutions against Extreme Flood and Severe Drought: Efficiency Evaluation of Risk Mitigation. *Climate Risk Management* **2023**, *40*, 100505, doi:10.1016/j.crm.2023.100505.
14. Guo, M.; Li, J.; Sheng, C.; Xu, J.; Wu, L. A Review of Wetland Remote Sensing. *Sensors* **2017**, *17*, 777, doi:10.3390/s17040777.
15. Simioni, J.P.D. Métodos de Classificação de Imagens de Satélite Para Delineamento de Banhados. Tese de Doutorado, Programa de Pós-Graduação em Sensoriamento Remoto, Universidade Federal do Rio Grande do Sul: Porto Alegre, 2021.
16. Berlanga-Robles, C.A. Trends in Mangrove Canopy and Cover in the Teacapan-Agua Brava Lagoon System (Marismas Nacionales) in Mexico: An Approach Using Open-Access Geospatial Data. *Wetlands* **2024**, *45*, 1, doi:10.1007/s13157-024-01877-6.
17. Machado-Machado, E.A.; Neeti, N.; Eastman, J.R.; Chen, H. Implications of Space-Time Orientation for Principal Components Analysis of Earth Observation Image Time Series. *Earth Sci Inform* **2011**, *4*, 117–124, doi:10.1007/s12145-011-0082-7.
18. Eastman, J.R. TerrSet Libera GIS. Eospatial Monitoring and Modeling System. Tutorial.; Clark University, 2024;
19. Korb, C.C. Hidrogeomorfologia de Áreas Úmidas Costeiras Com Uso de Sensoriamento Remoto, Parque Nacional Da Lagoa Do Peixe. Tese de Doutorado, Universidade Federal do Rio Grande do Sul, Programa de Pós-Graduação em Sensoriamento Remoto: Porto Alegre, 2025.
20. de Almeida, T.I.R.; Penatti, N.C.; Ferreira, L.G.; Arantes, A.E.; do Amaral, C.H. Principal Component Analysis Applied to a Time Series of MODIS Images: The Spatio-Temporal Variability of the Pantanal Wetland, Brazil. *Wetlands Ecol Manage* **2015**, *23*, 737–748, doi:10.1007/s11273-015-9416-4.
21. Pereira, L.E.; Noveli, R.A.P.; Filho, A.C.P. Uso de Análise de Componentes Principais (PCA) para Caracterização das Sub-Regiões do Megaleque do Taquari – Pantanal. *Revista GeoPantanal* **2023**, *18*, 114–126, doi:10.55028/geop.v18i34.18776.
22. Munyati, C. Use of Principal Component Analysis (PCA) of Remote Sensing Images in Wetland Change Detection on the Kafue Flats, Zambia. *Geocarto International* **2004**, *19*, 11–22, doi:10.1080/10106040408542313.
23. Torbick, N.; Becker, B. Evaluating Principal Components Analysis for Identifying Optimal Bands Using Wetland Hyperspectral Measurements From the Great Lakes, USA. *Remote Sensing* **2009**, *1*, 408–417, doi:10.3390/rs1030408.
24. Karabulut, M.; Küçükönder, M. An Examination of Temporal Changes in Göksu Delta (Turkey) Using Principle Component Analysis. *SSRN Journal* **2018**, doi:10.2139/ssrn.3457108.
25. Zhang, X.; Wang, G.; Xue, B.; Zhang, M.; Tan, Z. Dynamic Landscapes and the Driving Forces in the Yellow River Delta Wetland Region in the Past Four Decades. *Science of The Total Environment* **2021**, *787*, 147644, doi:10.1016/j.scitotenv.2021.147644.
26. Yelwa, S.A.; Sanda, A.B.; Usman, U. Spatio-Temporal Assessment of Vegetation Resource Dynamics in Nigeria from SPOT Satellite Imageries. *American Journal of Climate Change* **2019**, *8*, 502–519, doi:10.4236/ajcc.2019.84027.
27. Mattson, M.; Sousa, D.; Quandt, A.; Ganster, P.; Biggs, T. Mapping Multi-Decadal Wetland Loss: Comparative Analysis of Linear and Nonlinear Spatiotemporal Characterization. *Remote Sensing of Environment* **2024**, *302*, 113969, doi:10.1016/j.rse.2023.113969.
28. Dronova, I.; Gong, P.; Wang, L.; Zhong, L. Mapping Dynamic Cover Types in a Large Seasonally Flooded Wetland Using Extended Principal Component Analysis and Object-Based Classification. **2015**.
29. Vittorio, C.D.; Woessner, R. ISyE 6416 – Computational Statistics – Spring 2016 Final Project: "Big" Data Analytics Proposal.
30. Korb, C.C.; Guasselli, L.A.; Hasenack, H.; Belloli, T.F.; Cunha, C.S. Temporal and Spatial Variability of Hydrogeomorphological Attributes in Coastal Wetlands—Lagoa Do Peixe National Park, Brazil. *Coasts* **2025**, *5*, doi:10.3390/coasts5030023.
31. Schossler, V. Influência Das Mudanças Climáticas Em Geoindicadores Na Costa Sul Do Brasil. Tese de Doutorado, Programa de Pós-Graduação em Geociências, Universidade Federal do Rio Grande do Sul: Porto Alegre, 2016.

 doi:10.20944/preprints202605.0994.v1

32. Marengo, J.A.; Dolif, G.; Cuartas, A.; Camarinha, P.; Gonçcalves, D.; Luiz, R.; Silva, L.; Alvala, R.C.S.; SeluchiI, M.E.; Moraes, O.L.; et al. O maior desastre climático do Brasil: chuvas e inundações no estado do Rio Grande do Sul em abril-maio 2024. *Estud. av.* **2024**, *38*, 203–228, doi:https://doi.org/10.1590/s0103-4014.202438112.012.
33. Luerce, T.D.; Oliveira, G.G.; Guasselli, L.A.; Brubacher, J.P.; Figueiredo, A.R. Mapeamento geomorfológico a partir de dados SRTM: bacia hidrográfica do rio dos Sinos, RS.; Instituto Nacional de Pesquisas Espaciais (INPE), 2013; pp. 5210–5217.
34. IBGE. Manual técnico da vegetação brasileira: sistema fitogeográfico: inventário das formações florestais e campestres: técnicas e manejo de coleções botânicas: procedimentos para mapeamentos; IBGE: Rio de Janeiro, 2012; ISBN 978-85-240-4272-0.
35. Maltchik, L. (Org). Biodiversidade e Conservação de Áreas Úmidas Da Bacia Do Rio Dos Sinos; UNISINOS: São Leopoldo, 2003;
36. Costa, L.C.B. da; Guasselli, L.A. Dinâmica Sazonal de Remanescentes da Mata Atlântica a partir de séries Temporais NDVI/MODIS / Seasonal Dynamics of the Remaining Atlantic Forest, Froma a time series NDVI/MODIS. *Geo UERJ* **2017**, 214–239, doi:10.12957/geouerj.2017.15868.
37. Bazzan, T.; Rennó, C.D.; Lima, D.L.C.; Reckziegel, E.W. Integração da Incerteza na Amostragem e Classificação Random Forest Utilizando Bandas e Índices Espectrais para o Mapeamento de Inundação: Integration of Uncertainty in Sampling and Random Forest Classification Using Bands and Spectral Indices for Flood Mapping. *Geosciences = Geociências* **2022**, *41*, 905–925, doi:10.5016/geociencias.v41i04.16802.
38. Reboita, M.S.; Ambrizzi, T.; Rocha, R.P. da Relationship between the Southern Annular Mode and Southern Hemisphere Atmospheric Systems Relação Entre o Modo Anular Sul e Os Sistemas Atmosféricos No Hemisfério Sul. *Revista Brasileira de Meteorologia* **2009**, *24*, 48–55, doi:10.1590/S0102-77862009000100005.
39. Fontana, D.C.; Berlato, M.A. Influência do El Niño Oscilação Sul sobre a precipitação do Estado do Rio Grande do Sul. *Revista Brasileira de Agrometeorologia* **1997**, *5*, 127–132.
40. Korb, C.C.; Guasselli, L.A.; Belloli, T.F.; Cunha, C.S. Dinâmica espaço-temporal de pulsos de inundações nas Áreas Úmidas do Parque Nacional da Lagoa do Peixe, sul do Brasil. *Investigaciones Geográficas: Una mirada desde el sur* **2023**, 32–47, doi:10.5354/0719-5370.2023.71701.
41. Erthal, Douglas Bouvier Paisagem Urbana após Inundações de Setembro e Novembro de 2023 no Município de Roca Sales, , Rio Grande do Sul. *Boletim Geográfico do Rio Grande do Sul* **2024**, 78–101.
42. de Oliveira Andrades-Filho, C.; Mexias, L.F.S.; Quevedo, R.P.; Herrmann, P.B.; de Oliveira, G.G.; Cremon, É.H.; da Cargnin, B.R.; Reis, M. da S.; Novakoski, K.R.; dos Santos, D.C.; et al. The Biggest Landslide Event in Brazil: Preliminary Analysis of the Rio Grande Do Sul Mega Disaster in May 2024. *Landslides* **2025**, *22*, 3615–3624, doi:10.1007/s10346-025-02587-8.
43. SGB. Serviço Geológico do Brasil. Folha Porto Alegre SH-22 2026.
44. IBGE Banco de Dados e Informações Ambientais (BDIA). Mapeamento de Recursos Naturais (MRN), Escala 1:250 000 2023.
45. Streck, E.V.; Kämpf, N.; Dalmolin, R.S.D.; Klamt, E.; Nascimento, P.C.; Scheneider, P.; Giasson, E.; Pinto, L.F.S. *Solos Do Rio Grande Do Sul*; 2nd ed.; Emater-Ascar: Porto Alegre, 2008;
46. SEMA/FEPAM. Secretaria do Meio Ambiente e Infraestrutura/Fundação Estadual de Proteção Ambiental Hidrografia Ordem 2024.
47. Carlos M. Souza, J.; Shimbo, J.Z.; Rosa, M.R.; Parente, L.L.; Alencar, A.A.; Rudorff, B.F.T.; Hasenack, H.; Matsumoto, M.; Ferreira, L.G.; Souza-Filho, P.W.M.; et al. Reconstructing Three Decades of Land Use and Land Cover Changes in Brazilian Biomes with Landsat Archive and Earth Engine. *Remote Sensing* **2020**, *12*, doi:10.3390/rs12172735.
48. Ramos, R.A.; Pasqualeto, A.I.; Balbueno, R.A.; Das Neves, D.D.; De Quadros, E.L.L. Mapeamento e Diagnóstico de Áreas Úmidas No Rio Grande Do Sul, Com o Uso de Ferramentas de Geoprocessamento. In Proceedings of the Anais; 2014; pp. 17-21P.
49. ANA. Agência Nacional de Águas ANADEM – Modelo Digital de Terreno Para a América Do Sul 2018.

 doi:10.20944/preprints202605.0994.v1

50. SPGG.RS. Secretaria de Planejamento,Governança e Gestão do RS. Mancha de Inundação - Ano de 2024 2024.
51. Rouse, J.W.; Haas, R.H.; Schell, J.A.; Deering, D.W. Monitoring Vegetation Systems in the Great Plains with ERTS (Earth Resources Technology Satellite).; Greenbelt, 1973; pp. 309–317.
52. Wilson, E.H.; Sader, S.A. Detection of Forest Harvest Type Using Multiple Dates of Landsat TM Imagery. *Remote Sensing of Environment* **2002**, *80*, 385–396, doi:10.1016/S0034-4257(01)00318-2.
53. Xu, H. Modification of Normalised Difference Water Index (NDWI) to Enhance Open Water Features in Remotely Sensed Imagery. *International Journal of Remote Sensing* **2006**, *27*, 3025–3033, doi:10.1080/01431160600589179.
54. Guasselli, L. A.; Marques, D.L.M. Relações Entre as Estruturas de Fundo e Os Padrões Da Cobertura de Macrófitas Aquáticas No Banhado doTaim - RS. In Proceedings of the Anais; Goiânia-GO, 2006.
55. Sandi, S.G.; Rodriguez, J.F.; Saintilan, N.; Wen, L.; Kuczera, G.; Riccardi, G.; Saco, P.M. Resilience to Drought of Dryland Wetlands Threatened by Climate Change. *Sci Rep* **2020**, *10*, 13232, doi:10.1038/s41598-020-70087-x.
56. Nasution, H.; Yusfaneti, Y.; Saat, A. The Relationship Between Peat Water Content to Physical Properties of Peat at Various Ages of Oil Palm Plant and Year Products in Mekar Jaya Village. *Attractive : Innovative Education Journal* **2023**, *5*, 437–446, doi:10.51278/aj.v5i1.720.
57. Yang, Y.; Yin, J.; Slater, L.J.; Liu, P.; Zhang, L.; Zhang, Y. Global Vegetation Dynamics under Decreased Terrestrial Water Storage: Insights into Water Stress Response. *Agricultural and Forest Meteorology* **2025**, *368*, 110549, doi:10.1016/j.agrformet.2025.110549.
58. Tahsin, S.; Medeiros, S.C.; Singh, A. Assessing the Resilience of Coastal Wetlands to Extreme Hydrologic Events Using Vegetation Indices: A Review. *Remote Sensing* **2018**, *10*, doi:10.3390/rs10091390.
59. Liu, Q.; Gan, L.; Wu, H.; Liang, L.; Yan, D.; Wang, X.; Li, C.; Sun, T. Water Level Fluctuations Control Wetland Hydrological Connectivity in Driving the Integrity of Wetlands. *Journal of Hydrology* **2025**, *657*, 133095, doi:10.1016/j.jhydrol.2025.133095.
60. Nepita-Villanueva, M.R.; Berlanga-Robles, C.A.; Ruiz-Luna, A.; Morales Barcenas, J.H. Spatio-Temporal Mangrove Canopy Variation (2001–2016) Assessed Using the MODIS Enhanced Vegetation Index (EVI). *J Coast Conserv* **2019**, *23*, 589–597, doi:10.1007/s11852-019-00689-9.
61. Wang, Y.; Jin, S.; Dardanelli, G. Vegetation Classification and Evaluation of Yancheng Coastal Wetlands Based on Random Forest Algorithm from Sentinel-2 Images. *Remote Sensing* **2024**, *16*, 1124, doi:10.3390/rs16071124.
62. Padovani, C.R. Dinâmica Espaço-Temporal Das Inundações Do Pantanal. Tese de Doutorado, Ecologia de Agroecossistemas, Universidade de São Paulo: Piracicaba, 2010.
63. Duhalde, D.; Cortés, J.; Arumí, J.-L.; Boll, J.; Oyarzún, R. Exploring the Behavior of the High-Andean Wetlands in the Semi-Arid Zone of Chile: The Influence of Precipitation and Temperature Variability on Vegetation Cover and Water Quality. *Water* **2024**, *16*, doi:10.3390/w16243682.
64. Thamaga, K.H.; Dube, T.; Shoko, C. An Assessment of Small Wetland Ecohydrological Dynamics Using Sentinel-2 MSI Derived Spectral Indices in Semi-Arid Environments of South Africa 2021.
65. Ashok, A.; Rani, H.P.; Jayakumar, K.V. Monitoring of Dynamic Wetland Changes Using NDVI and NDWI Based Landsat Imagery. *Remote Sensing Applications: Society and Environment* **2021**, *23*, 100547, doi:10.1016/j.rsase.2021.100547.
66. Gizaw, M.S.; Gan, T.Y. Impact of Climate Change and El Niño Episodes on Droughts in Sub-Saharan Africa. *Clim Dyn* **2017**, *49*, 665–682, doi:10.1007/s00382-016-3366-2.
67. Waddington, J.M.; Morris, P.J.; Kettridge, N.; Granath, G.; Thompson, D.K.; Moore, P.A. Hydrological Feedbacks in Northern Peatlands. *Ecohydrology* **2015**, *8*, 113–127, doi:10.1002/eco.1493.

 doi:10.20944/preprints202605.0994.v1

68. Golden, H.E.; Sander, H.A.; Lane, C.R.; Zhao, C.; Price, K.; D'Amico, E.; Christensen, J.R. Relative Effects of Geographically Isolated Wetlands on Streamflow: A Watershed-Scale Analysis. *Ecohydrology* **2016**, *9*, 21–38, doi:10.1002/eco.1608.
69. Leibowitz, S.G.; Wigington Jr., P.J.; Schofield, K.A.; Alexander, L.C.; Vanderhoof, M.K.; Golden, H.E. Connectivity of Streams and Wetlands to Downstream Waters: An Integrated Systems Framework. *JAWRA Journal of the American Water Resources Association* **2018**, *54*, 298–322, doi:10.1111/1752-1688.12631.